🔓 Open Access

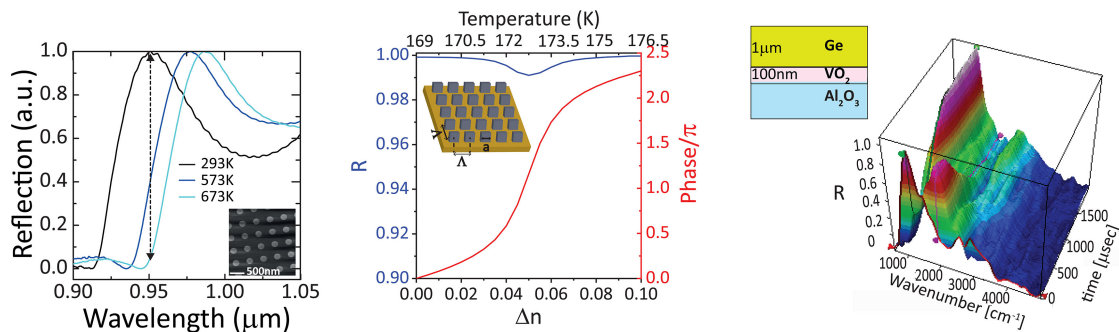# Thermally Reconfigurable Meta-Optics

Tomer Lewi
Nikita A. Butakov
Hayden A. Evans
Mark W. Knight
Prasad P. Iyer
David Higgs
Hamid Chorsi
Juan Trastoy
Javier Del Valle Granda
Ilya Valmianski
Christian Urban
Yoav Kalcheim
Paul Y. Wang
Philip W.C. Hon
Ivan K. Schuller
Jon A. Schuller

Thermally Reconfigurable Meta-Optics

Tomer Lewi [ORCID],[1] Nikita A. Butakov,[2] Hayden A. Evans,[3]
Mark W. Knight,[4] Prasad P. Iyer,[2] David Higgs,[2] Hamid Chorsi,[2]
Juan Trastoy,[5,6] Javier Del Valle Granda,[5] Ilya Valmianski,[5]
Christian Urban,[5] Yoav Kalcheim,[5] Paul Y. Wang [ORCID],[5]
Philip W.C. Hon,[4] Ivan K. Schuller,[5] and Jon A. Schuller[2]

[1]Faculty of Engineering and Institute for Nanotechnology and Advanced Materials, Bar-Ilan University, Ramat-Gan 5290002, Israel
[2]Department of Electrical and Computer Engineering, University of California Santa Barbara, Santa Barbara, CA 93106 USA
[3]Materials Research Laboratory and the Department of Chemistry and Biochemistry, University of California Santa Barbara, CA 93106 USA
[4]NG Next Northrop Grumman Corporation, Redondo Beach, CA 90278 USA
[5]Department of Physics, University of California, San Diego, La Jolla, CA 92093 USA
[6]Unité Mixte de Physique CNRS, Thales, Université Paris-Sud, Univ. Paris Saclay, Palaiseau 91767, France

Abstract: Metasurfaces are two-dimensional nanostructures that allow unprecedented control of light through engineering the amplitude, phase, and polarization across meta-atom resonators. Adding tunability to metasurface components would boost their potential and unlock a vast array of new application possibilities such as dynamic beam steering, tunable metalenses, and reconfigurable meta-holograms, to name a few. We present here high-index meta-atoms, resonators, and metasurfaces reconfigured by thermal effects, across the near to mid-infrared spectral ranges. We study thermal tunability in group IV and group IV–VI semiconductors, as well as in phase-transition materials, and demonstrate large dynamic resonance frequency shifts accompanied by significant amplitude and phase modulation in metasurfaces and resonators. We highlight the importance of high-Q resonances along with peak performance of thermal and thermo-optic effects, for efficient and practical reconfigurable devices. This paper paves the way to efficient high-Q reconfigurable and active infrared metadevices.

Index Terms: Dielectric resonator antennas, nanophotonics, nanoparticles, nanostructured materials, optical metamaterials, phase change materials, semiconductor materials, thermooptical devices.

1. Introduction

Metasurfaces are planar ordered optical structures composed of subwavelength resonators, designed to manipulate light through arbitrary wavefront shaping [1]–[4]. Recently, the all-dielectric metasurface approach [2] has led to tremendous progress, giving rise to several dielectric metasurface demonstrations including achromatic and broadband metalenses [5]–[7], axicon lenses [8], sub-diffraction focusing [9], nonlinear generation [10]–[12] beam deflectors [8], [13], [14], wave plates and beam converters [15]–[18], holograms [19], [20], [21], antireflection coatings [22] and magnetic mirrors [23], to name a few. So far, however, most metasurfaces are implemented for static operation and optimized for limited bandwidth of operation. The next level lies in dynamic and active control over light, which will drastically increase metasurface capabilities and potential applications.

The fundamental challenge for achieving reconfigurable operation is to obtain large and continuous modulation of optical properties within subwavelength meta-atoms and meta-molecules which are inherently low-Q resonators [24], [25]. Desirable tuning mechanisms continuously shift the resonance frequency of the metastructure with at least one linewidth of the resonance, thus allowing to maximize the modulation of both amplitude and phase. These challenges have motivated several studies exploring different approaches, designs, and materials that provide extreme tunability. Previous investigations of active tuning in dielectric metasurfaces and meta-atoms have focused on ultrafast free-carrier injection [26]–[30], coupling to liquid crystals [31], [32], to atomic vapor [33] or to ENZ materials [34], [35], phase change materials [36]–[38] and MEMS [39]–[41]. However, most of these approaches do not provide a viable solution for a fully reconfigurable metadevice where at each subwavelength meta-atom the phase and amplitude can be individually and continuously tuned to provide an arbitrary phase profile. Recent studies have showed that the thermo-optic effect (TOE), i.e., refractive index variation with temperature dn/dT can be used to induce large and continuous index shifts in materials having extraordinary thermal dependence [42]–[44]. The TOE was also recently used to actively tune Si metasurfaces, but only at a limited temperature range (273–573 K) [45]. Here we study thermal tunability in several groups of high-index semiconductor resonators, over large temperature and spectral ranges. We demonstrate thermal tuning of Mie resonances due to the normal positive TOE ($dn/dT > 0$) and the anomalous negative TOE ($dn/dT < 0$). The latter is achieved in two different cases; the first is due to thermal excitation of free carriers (FC) in group IV semiconductors (Si and Ge) at elevated temperatures, where the free carrier response dominates over the normal positive TOE; the second is achieved in the lead chalcogenide family of group IV-VI semiconductors (PbTe) where the material itself exhibits a large and anomalous thermo-optic coefficient (TOC) [42], driven by its anomalous bandgap dispersion with temperature. We also demonstrate the tuning of high order mid-infrared MIR Mie resonances by several linewidths with a temperature swings as small as $\Delta T < 10$ K. We exploit the large TOC of Si at near-infrared (NIR) wavelengths to realize optical switching and tunable metafilters. Lastly, we discuss reconfigurable and switchable devices driven by metal-insulator transitions in vanadium-oxide (VO_2). We demonstrate independent and continuous tuning of both amplitude and phase in a single electrically controlled nanophotonic device based on Ge on VO_2.

Thermo-optic (TO) effects provide an ideal test bed for demonstrating and elucidating reconfigurable metasurface properties. TO tuning can provide large index shifts with no added losses and be integrated into electrically-controlled architectures [46], [47]. Thus, TO tunability forms the basis for many reconfigurable integrated photonic devices [46]–[49]. However, the TOC of most materials is small for subwavelength applications, hence typical TO applications exploit small index changes acting over distances much larger than a wavelength to achieve useful modulation. For efficient modulation of subwavelength resonators, the maximally induced index shift Δn should tune the resonance wavelength by more than its linewidth ($\Delta\lambda/FWHM > 1$, where $\Delta\lambda$ is the resonance wavelength shift and FWHM is the full width at half max of the linewidth). The route for achieving this tunability is by maximizing the TOE using extraordinary materials [42], [43], [50], [44] and/or narrowing the resonance linewidth using high-Q modes [42] such as supported by asymmetric [32] or fano-resonant [10] metasurfaces. Here, we first study the TO tuning capabilities of Si and Ge
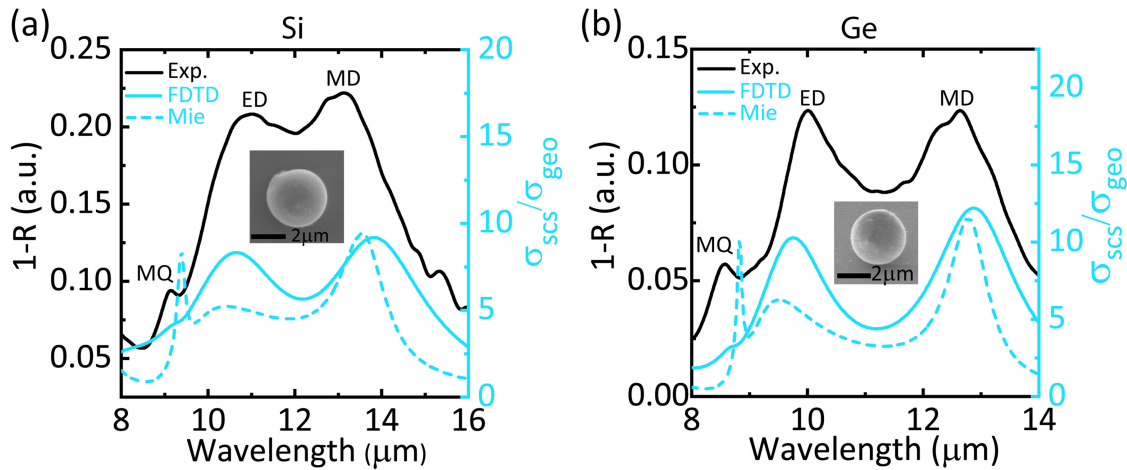
Fig. 1. Single semiconductor Mie resonator meta-atoms (a) Si spherical Mie resonator, d = 3.8 μm and (b) Ge spherical Mie resonator, d = 3.075 μm. Experimental spectra (black) show good agreement with the calculated Mie scattering (cyan, dashed) and FDTD (solid cyan) cross-sections σ_{sca} normalized to the geometric cross-section σ_{geo}. A series of multipolar resonance peaks are visible in the spectra and correspond to magnetic dipole (MD), electric dipole (ED) and magnetic quadrupole (MQ), respectively.

− the most commonly used materials for dielectric metasurfaces and nanophotonics. The TOC of these semiconductors are amongst the highest of natural materials [51] which, along with their high refractive indices and CMOS compatibility, makes them very attractive materials for reconfigurable metasurfaces. However, the typical TOC values ($\sim 1 - 5 \times 10^{-4}$ K^{-1}) requires large temperature modulation which may cause problems if the TOC is strongly temperature dependent [42], [43]. In the MIR range, for instance, working at high temperatures can generate FC densities in semiconductors that dramatically alter the optical constants due to Dude-like dispersion [52]. The total induced index shift of the semiconductor due to a *positive* temperature gradient is the sum of contributions from the normal TO effect and the thermal FC effect: $\Delta n = \Delta n_{TO} + \Delta n_{FC}$. In vast majority of materials, the TOC is positive hence $\Delta n_{TO} > 0$ while the FC term has a negative contribution $\Delta n_{FC} < 0$ (due to the plasma frequency blue shift caused by FCs, in a Drude model). The thermal FC term (Δn_{FC}) is particularly strong for low bandgap semiconductors with small effective masses [24], [42], [43], but in most semiconductors is negligible below ~ 500 K.

2. Results and Discussion

This study of thermal tunability is mainly focused for the MIR spectral range which has tremendous scientific and technological interest including nanospectroscopy [53], thermal imaging [54], chemical and biological sensing [55]–[58], medical applications [59], laser countermeasures [60] and spectro-interferometry for astro-photonics [61]–[66], to name a few. Importantly, thermal tunability can be extended to the NIR and visible ranges where the performance of e.g., Si and Ge, can be improved due to the expected increase of dn/dT at shorter wavelengths.

2.1 Group IV Semiconductors

To investigate thermal tunability and assess its capabilities, we start by studying Si and Ge single spherical meta-atom resonators fabricated by laser ablation [24], [67]. The TO coefficients of these semiconductors are amongst the highest of natural materials [51] which, along with their high refractive indices and CMOS compatibility, makes them very attractive materials for reconfigurable metasurfaces. Examples of Si (r = 1.9 μm) and Ge (r = 1.54 μm) meta-atom Mie resonators are illustrated in Figures 1a and 1b. The first three multipolar Mie resonances in the range 8–14 μm are

observed using both analytical calculations (cyan dashed), FDTD simulations (cyan), and single particle infrared microspectroscopy (black). These multipolar resonances are labeled according to their polarization (Magnetic or Electric) and mode order (Dipole, Quadrupole). The challenge to obtain sufficient resonance tuning is illustrated in Figure 2. Temperature dependent spectra of these resonators (80–873K for Si and 123–773K for Ge) are presented in Figures 2a and 2b. Spectral shifts are observed for all resonances as a response to the thermal modulation of the refractive index of the resonators. However, the observed red shifts of resonances are insufficient to allow tuning by one resonance linewidth. Moreover, the expected gradual red shift of the dipole modes in both Si and Ge at low and moderate temperatures, plateaus at elevated temperatures then followed by blue shift of resonances at high temperatures. This effect is more pronounced in the Ge resonator and for the longer MIR wavelengths.

The origin of this behavior is revealed in Figures 2c and 2d, where the chromatic dispersion and temperature dependence of dn/dT is plotted for the two materials. The reason for this peculiar behavior of the TOC can be explained when taking into account thermally generated free carriers (FCs) [52]. Neglecting all other secondary effects of temperature (such as effective mass, mobility, band structure changes etc'.), the explicit form of the temperature dependent permittivity can be written as:

$$\varepsilon(T) = n(T)^2 = \varepsilon_{\infty,\text{TO}}(T) - \frac{\omega_p^2(T)}{\omega^2 + i\gamma\omega} \qquad (1)$$

where the first term on the right hand side, $\varepsilon_{\infty,\text{TO}}$, is responsible for the normal TOE with no FC effects, and the second term is the free carrier contribution with the plasma frequency ω_p, the damping coefficient γ, and scattering time τ are defined as $\omega_p = \sqrt{\frac{n_i e^2}{m_c \varepsilon_0}}$ and $\frac{1}{\gamma} = \tau = \frac{\mu m_c}{e}$, n_i is the intrinsic free carrier concentration (not to be confused with the refractive index n), e is the electron charge, m_c is the conductivity effective mass, ε_0 and ε_∞ are the permittivity of free space and the high frequency permittivity, respectively, and μ is the free carrier mobility.

For low and intermediate temperatures, the density of thermally generated FCs is negligible ($n_i < 10^{17}$ cm^{-3}), and thus all resonances in figure 2a and 2b red shift in response to a positive thermal gradient due to the normal positive dn/dT in both Si and Ge. At elevated temperatures (T > 550 K), significant amount of intrinsic FCs are generated which tends to decrease the refractive index according to Eq. (1). This effect is more pronounced for low bandgap materials [52] and hence has a larger influence on the Ge resonances, due to the lower bandgap of Ge (E_g = 0.66eV @ T = 300 K) compared to Si (E_g = 1.126eV @ T = 300 K) and lower effective mass [24]. Finally, at high temperature T > 700 K, the effect of thermal FCs dominates over the normal (positive) TO effect and leads to an anomalous negative TOC (dn/dT < 0), as seen in figures 2c and 2d.

In Figures 2e and 2f we track the temperature dependent resonance wavelength shifts of the MD and ED, with respect to the RT resonance wavelength, and extract the corresponding index shifts $\triangle$n. Using our model for the temperature dependent permittivity (Eq. 1), we compare experiments to calculated resonance and index shifts of the ED and MD modes. For Si, the curvature of dn/dT significantly changes only above ∼750 K and exclusively for the MD mode (due to its longer wavelength), as seen by the peak in both $\triangle$n and $\triangle\lambda$ at∼800 K. Above the peak, the induced index and resonance wavelength decrease due to the generation of $n_i > 10^{17}$cm^3 free carriers; the sign of dn/dT has reversed (dn/dT <0, Figure 2c) and now causes a slight blue shift for the MD mode (at this point the curvature of the ED mode is also affected as it starts to flatten).

For the Ge resonator (Figure 2f), FC effects are more prominent and emerge at lower temperatures. Due to its smaller bandgap and lower effective masses, the dispersion of the induced index $\triangle$n of the MD mode starts to flatten at ∼550 K, peaks at 600 K then decreases at higher temperatures (dn/dT < 0). For even more elevated temperatures free carriers dominate the index change giving rise to a larger magnitude $\lvert$dn/dT$\rvert$. The behavior of the ED is similar, but the change in curvature of $\triangle$n is shifted to higher temperature T ∼ 675 K since the FC effect is smaller at shorter wavelengths. Altogether, these results show that the dispersion, the sign, and magnitude of dn/dT can be controlled with temperature in low and moderate bandgap semiconductor resonators through
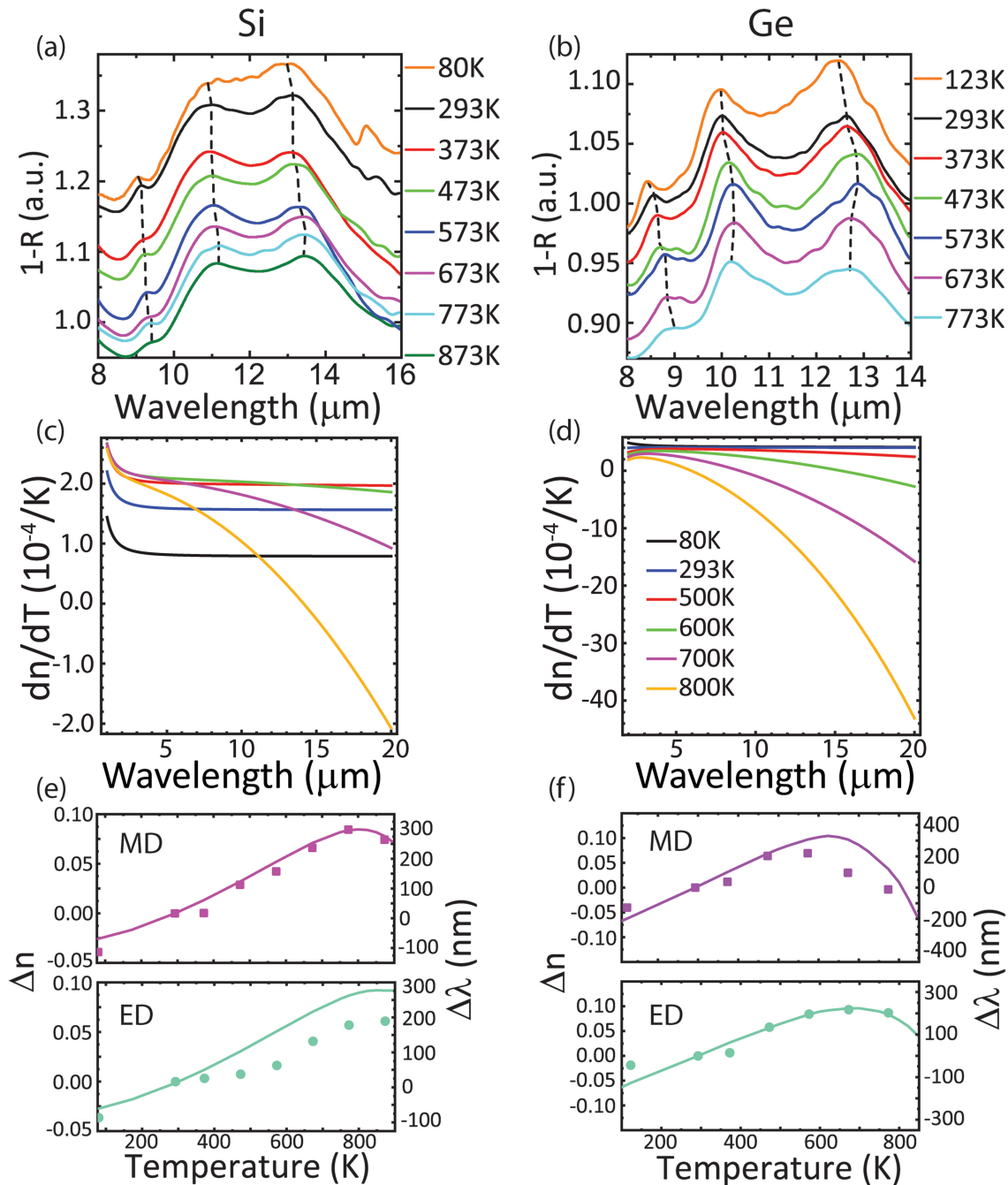
Fig. 2. Thermal tunability in single semiconductor meta-atom resonators. (a) & (b) Temperature dependent spectra of the spherical resonators of figure 1, between 80 K and 900 K. The spectral shifts of magnetic and electric dipole (MD and ED) and magnetic quadrupole (MQ) modes are highlighted. The dashed lines track the temperature dependent resonance peaks and are a guide to the eye. (c) & (d): Calculated chromatic dispersion of dn/dT at various temperatures in Si (c) and Ge (d). Each color plot corresponds to dn/dT at different temperature as detailed in the legend of (d). (e) & (f): The extracted induced index and resonance wavelength shifts as a function of temperature for MD and ED modes in Si (e) and Ge (f). Dots are experimentally extracted values while solid lines are calculated shifts based on Mie theory.
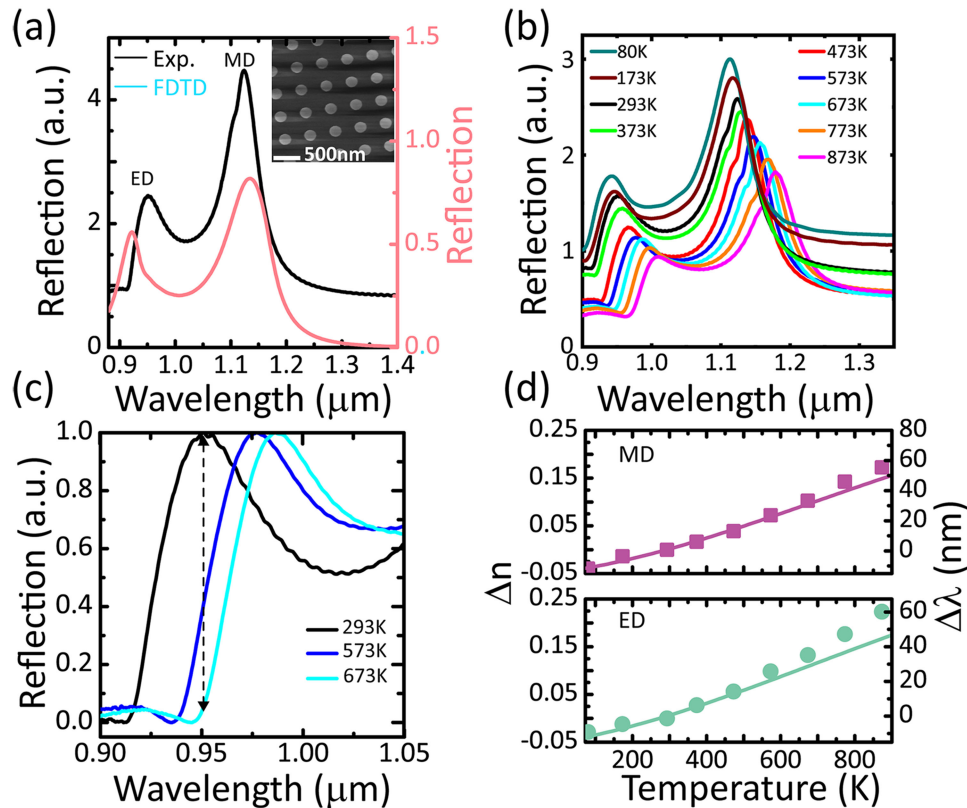
Fig. 3. Thermally reconfigurable Si metasurfaces. (a) RT Reflection spectra of a Si metasurface disk array with disk diameter and height of d = 290 nm and h = 280 nm respectively and periodicity a = 590 nm on a SiO2 substrate. Experimentally measured (black) and FDTD (red) spectra are in good match showing the fundamental MD and ED modes. The inset presents an SEM image of the metasurface. (b) Temperature-dependent Reflection spectra exhibiting continuously red-shifted MD and ED resonances with increasing temperature. The spectra are vertically shifted along the y-axis for visibility. (c) Thermally reconfigurable metafilter demonstration, exhibiting 4 dB and 13 dB amplitude modulation when temperature gradients of △T = 280 K and △T = 380 K, are applied, respectively. (d) Thermally induced index and wavelength shifts of MD and ED modes.

the generation of free carriers. This can be used to engineer the dispersion of dn/dT and for tuning of infrared meta-atoms, thermal emitters and resonators.

A different route for increasing the TO normalized tunability is to exploit the larger TOC at shorter wavelengths, in the vicinity of the material bandgap. As seen in Figure 2c, the dn/dT values are up to 50% larger in Si around 1 μm. Next, we demonstrate thermally reconfigurable Si metasurfaces utilizing the increased TOC at NIR wavelengths. Figure 3a shows experimental and FDTD reflection spectra of a silicon disk array on a SiO$_2$ substrate, with disk diameter and height of d = 290 nm and h = 280 nm respectively, and periodicity a = 590 nm. Both experimental and FDTD spectra show pronounced MD and ED resonances (Q $\sim$ 21) at λ = 1.12 μm and λ = 0.95 μm, respectively. Experimental temperature dependence of these resonances is presented in Figure 3b (the spectra are vertically shifted along the y-axis for visibility), where both dipole modes are continuously red shifted with increasing temperatures. The extracted index and resonance wavelengths shifts △n and △λ are presented in figure 3d for both dipole modes (△n and △λ are calculated with respect to index and resonance wavelengths values at RT). The higher TOC at shorter wavelengths is evinced by the larger induced index shift △n for the ED mode compared to the MD mode. These high dn/dT values at the ED resonance wavelengths, combined with relatively narrow linewidths (Q $\sim$ 21), allows for tunable metafilter operation (Figure 3c) with amplitude modulation of more than
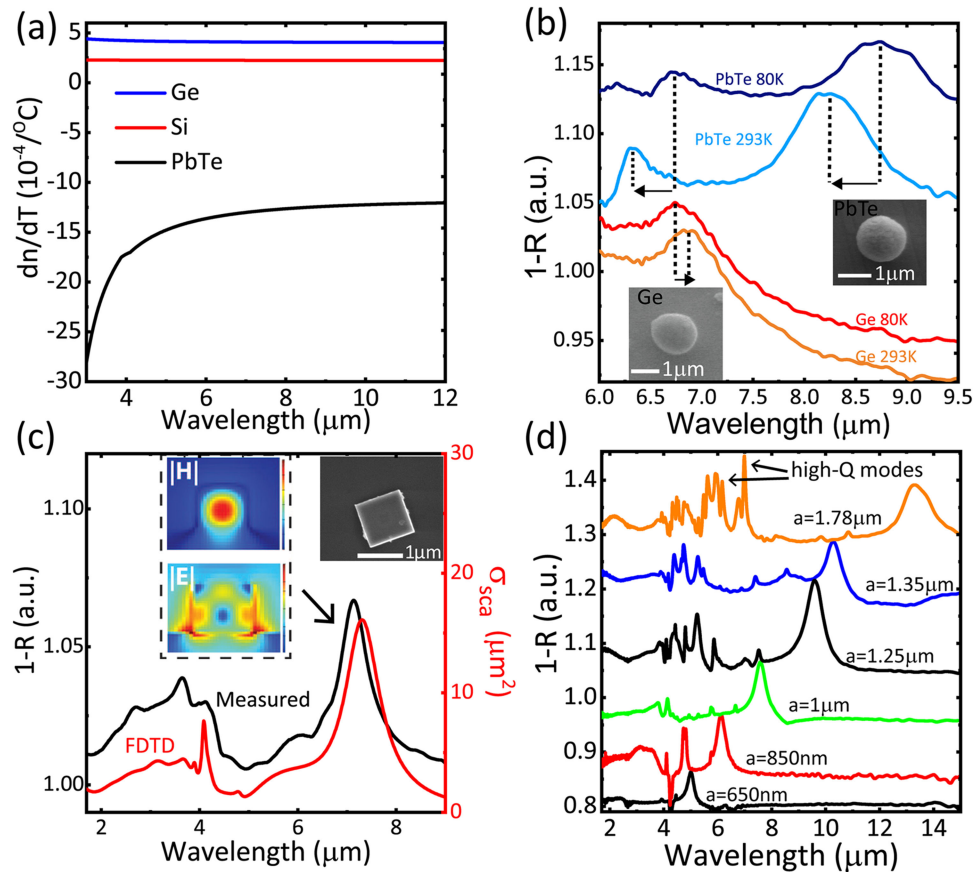
Fig. 4. Large TO tuning in PbTe single resonators. (a) TO coefficient of Ge, Si and PbTe at RT. (b) TO induced shift between 80 K and 293 K in a d = 1.45 μm PbTe sphere compared to a d = 1.7 μm Ge sphere. The combination of a higher Q and larger TOC enables far greater tunability in PbTe, as evinced by the linewidth of resonance shifting in the dipole modes. (c) Solution processed cubic PbTe resonator of side a = 1 μm, on a Si substrate. The insets show an SEM image of the cubic particle along with the electric and magnetic field profiles of the fundamental MD mode. (d) Geometric dispersion of PbTe cubes on gold, demonstrating resonance scaling with size. The spectra are shifted along the y-axis for visibility. High order resonances exhibiting very high Q-factors (Q $\sim$ 60) emerge for the larger cubes (Orange lines).

95% (13 dB) for $\Delta T = 380$ K at $\lambda = 950$ nm. Importantly, thermal tunability in Si metasurfaces can be extended to the visible range, with improved performance due to the expected increase of dn/dT at shorter wavelengths.

2.2 Group IV-VI Semiconductors

Although TOCs of group-IV Si and Ge are amongst the highest of natural materials [51], achieving the desired tunability ($\Delta\lambda$/FWHM > 1) in Si and Ge metasurface requires large temperature gradients. Meeting the desired linewidth tunability with relaxed temperature modulation, requires materials with higher TOCs and/or narrowing the resonance linewidth. Remarkably, the lead chalcogenide family PbX (X = S, Se, Te) possesses both very large refractive indices with highest reported values of TOCs (figure 4a). Interestingly, the sign of the TOC is negative (dn/dT < 0) due to anomalous temperature-dependent bandgap dispersion [51], [68], [69]. For example, experimental measurements of temperature-dependent Ge and PbTe Mie resonances are shown in figure 4b. Ge has the highest reported (positive) TOC of any semiconductor outside the lead chalcogenide family and is therefore compared here to PbTe. In comparison with Ge, two important characteristics can

be observed regarding PbTe, both arising from the larger refractive index ($n_{PbTe}\sim6$, $n_{Ge}\sim4$). First, although the PbTe sphere size is smaller, resonances occur at longer wavelengths with higher calculated scattering efficiencies. Secondly, all PbTe resonances exhibit higher Qs than their Ge counterparts. In going from 80 K (red) to 293 K (orange) the Ge MD mode red-shifts by 90nm. Dividing by the linewidth (FWHM), this corresponds to a normalized tuning of $\Delta\lambda$/FWHM $= 0.09$. In comparison, the same temperature swing causes a significantly larger *blue-shift* (480nm), and normalized tuning $\Delta\lambda$/FWHM $= -0.65$ in PbTe MD mode. Furthermore, the normalized tunability of the PbTe ED mode is $\Delta\lambda$/FWHM $= -1.5$ due to the narrower linewidth of this resonance. These results clearly demonstrate the strong, negative TO effect in PbTe nanoparticles and is the largest dynamic tuning of Mie resonators reported to date [26]–[28], [31]. These properties make PbTe an ideal candidate material for TO-tunable nanophotonics and metasurface resonators.

PbTe provides another intriguing benefit: solution-processable high Q-factor subwavelength resonators. For instance, solution processed PbTe photovoltaics [70] and thermoelectrics [71] have already been demonstrated. Using solution processing [42] we synthesize cube-shaped crystalline PbTe resonators with sizes ranging between 0.3–3 μm. Solution-processing provides a low cost and straightforward method to obtain a large quantity of resonators that can be easily deposited on any substrate. An SEM (inset) and infrared spectra of an example PbTe resonator cast on a Si substrate are shown in figure 4c. The resonator exhibits a set of Mie resonances in experiments (black) and simulations (red) analogous to that of spherical particles. For instance, simulated field profiles (inset) confirm that the fundamental resonance at $\lambda = 7.13$ μm is an MD-like mode. Similarly, the extracted linewidth (Q$\sim$10) of the MD mode is comparable to that of spherical resonators. The spectra for PbTe cubes of varying sizes casted on gold surface are shown in Figure 4d. The interaction with mirror images [72] produces higher Q-factor resonances and also shifts all resonances to longer wavelengths. All the resonance features in Figure 4d exhibit expected linear size dispersion, allowing to size-based engineering of high quality resonances across the PbTe infrared transparency range. Numerous high-Q (Q $\sim$ 60) higher-order modes can also be seen, especially in larger cubes.

Figure 5a summaries the TO tunability between 80 K and RT of dipole modes for various PbTe resonators discussed above (sphere in figure 4b, cube on Si in figure 4c and the a $=$ 850 nm cube on Au from Figure 4d (red line)). All resonances exhibit blue shift normalized tunability of the order of unity with the largest value of $\Delta\lambda$/FWHM $= -1.5$ obtained by the ED mode of the spherical particle. Tracking the shift of all Mie resonances across a variety of temperatures provides valuable insight into the dispersion of TOE with temperature and wavelength. The temperature dependence of the MD (red) and ED (green) resonance wavelengths of the d $= 1.45$ μm sphere along with the MD (blue) and buried MD (purple) modes of the a $= 1$ μm PbTe cube on Si, are plotted in Figure 5b. The tunable resonances exhibit some unusual characteristics. The wavelength shifts at low temperatures (80 K–293 K) are much larger than the shifts above room temperature (293 K–573 K), as evidenced by the differences in slopes of all modes seen in Figure 5b. These results show that the largest dn/dT occurs between 80 K to RT and a more thorough examination reveals a maximum in dn/dT somewhere between 80 K and 200 K [42]. Although observed shifts are consistent with other measurements [68], [73], [74], this significant increase in TO coefficient at low temperatures has not previously been reported. Moreover, standard TO models [51], based on temperature-dependent bandgap (E_g) dispersion, [69], [75] are unable to explain this effect, suggesting unknown physical mechanisms may be at play. Nevertheless, by operating at cryogenic temperatures, significant increases in TO tunability can be achieved.

Combining the large low-temperature TOE with high-Q resonances enables complete tuning (i.e., by more than one linewidth) of resonances with significantly reduced temperature swings (ΔT). Due to its high index and negligible losses, high-Q resonances are observed in single PbTe cubic (figure 4d) and spherical and resonators (Figure 6a). TO spectral tuning of a high order high-Q (Q $\sim$ 100) resonance of a d $= 1.76$ μm PbTe sphere is shown in Figure 6a. This sharp resonance can be tuned by more than one linewidth (normalized tunability $= 1.6$) with a temperature swing as small as ΔT $= 10$ K. This exceptional tunability is enabled by the combination of the narrow linewidth
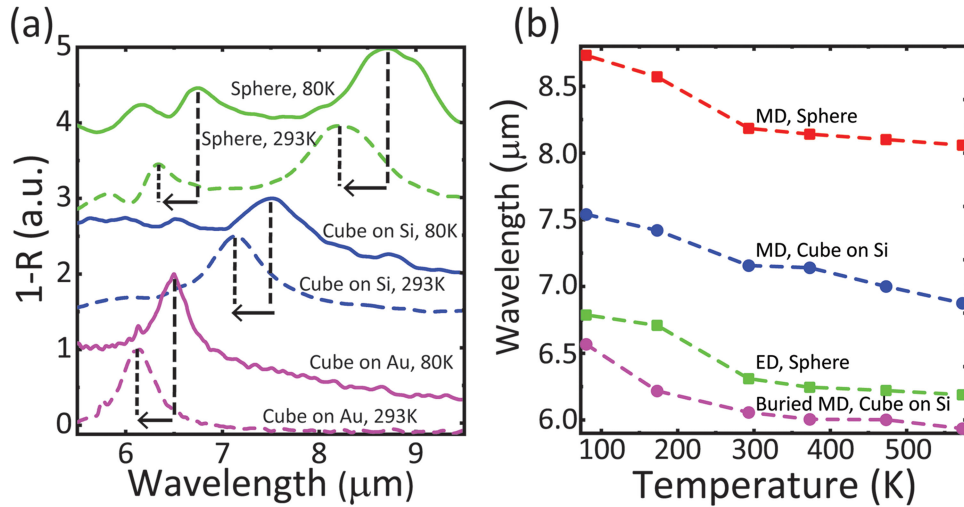
Fig. 5. Dynamic tuning using the anomalous TO effect in PbTe resonators. (a) TO induced shift between 80 K and 293 K in i) MD and ED modes of the d = 1.45 μm PbTe sphere presented in figure 4b (green solid and dashed lines). The normalized tuning of the ED modes is $\Delta\lambda$/FWHM = 1.5 (ii) The a = 1 μm PbTe cube on Si presented in figure 4c (blue solid and dashed lines) and (iii) PbTe cube of side a = 850 nm on gold (pink solid and dotted lines). The combination of a high Q and large TO coefficient enables large tunability of the fundamental MD mode in PbTe culminating in a normalized tunability of 1.15 (for ΔT = 80–293 K) for the cubic resonator on gold. (b) Temperature dependent multipolar resonance shifts of the MD (red) and ED (green) modes in the d = 1.45 μm PbTe sphere along with the MD and buried MD modes of the a = 1 μm PbTe cube on Si. The dashed lines are a guide to the eye. Resonance shifts exhibit the large and anomalous (dn/dT < 0) TO coefficient, and a marked increase in magnitude below room temperature.
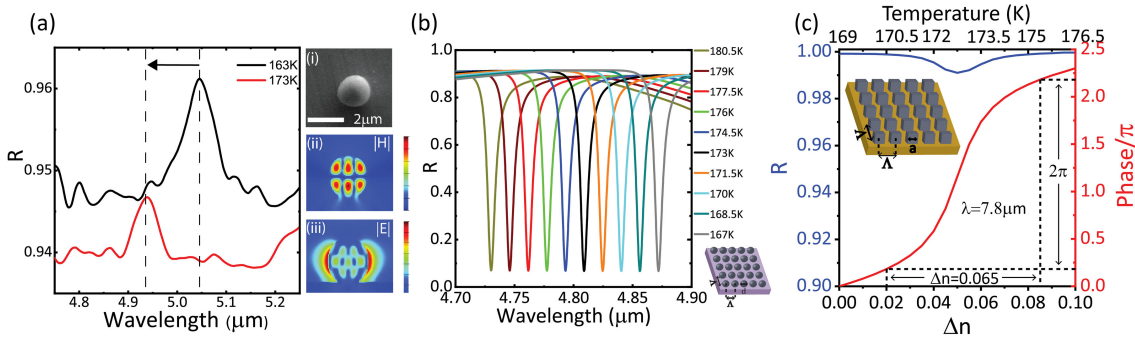

Fig. 6. Ultra-high tunabilty in subwavelength PbTe metasurfaces. (a) Experimental demonstration of TO tuning of high order high-Q resonances in single PbTe spherical particles by more than a linewidth with ΔT = 10 K. The normalized tunabiltiy is $\Delta\lambda$/FWHM = 1.6. (b) Reflection FDTD simulation of a cubic spherical metasurface array (sphere diameter d = 1.8 μm and periodicity Λ = 2 μm), exhibiting a sharp resonance dip which is thermo-optically tuned with ΔT = 1.5 K intervals. Reflection dips are shifted by more than a linewidth (normalized tunability = 1.975) with Δn = 0.02—steps that corresponds to ΔT = 1.5 K intervals around T = 173 K. (c) Reflection and phase FDTD simulation at λ = 7.8 μm vs induced index Δn and temperature in cubic PbTe metasurface comprising PbTe cubes of side a = 1.78 μm on (PEC) substrate with periodicity of Λ = 2 μm. More than 2π phase shift is achieved with greater than 99% reflectivity and $\Delta n \leq 0.065$ using temperature swing of $\Delta T \sim$ 5 K.

and peak TOE. The observed dn/dT at 173 K (-0.0134 K^{-1}) is almost an order of magnitude larger than previously reported RT TO effects [51] (dn/dT = -0.0015K^{-1}).

The potential to exploit widely tunable PbTe meta-atoms in reconfigurable metasurfaces is illustrated in Figure 6b. Simulated reflection spectra of a metasurface comprising subwavelength 2D array of spheres (diameters of d = 1.76 μm and periodicity Λ = 2 μm) on a PbTe substrate are

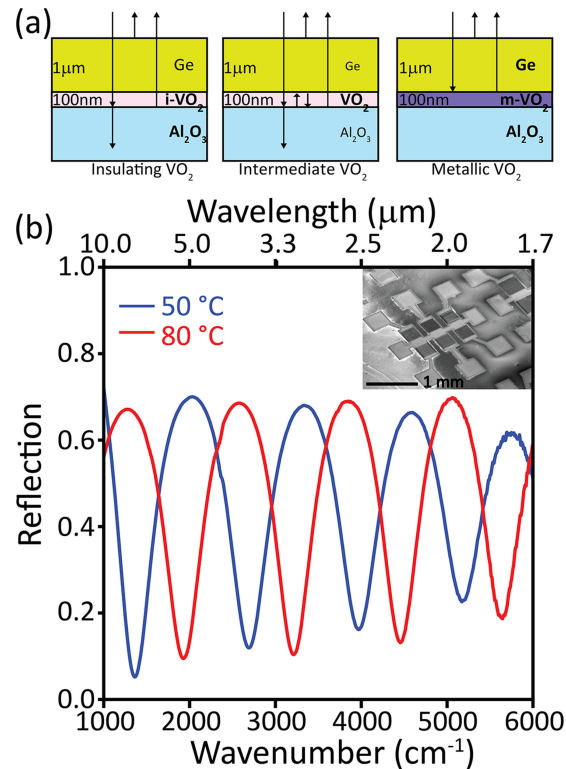Fig. 7. Temperature-tunable Fabry–Pérot resonator. (a) Schematic of Ge–VO$_2$–Al$_2$O$_3$ device in the insulating, intermediate, and metallic states. The arrows represent the dominant reflection interfaces. (b) Experimentally measured reflectivity, of a 1 μm thick Ge Fabry–Pérot cavity, on a 100 nm thick film of VO$_2$, on an R-cut sapphire substrate.

shown in Figure 6b. Reflection dips of ∼90% can be observed due to coupling to the single-particle high-Q mode shown in Figure 6a. Additionally, inter-particle coupling leads to resonance linewidth narrowing and much higher Qs are obtained (Q ∼ 600). These high Q resonances now allow more than a linewidth of tunability (normalized tunability of 1.975) with an induced index shift of $\Delta n = 0.02$. This induced index change corresponds to a temperature span of just $\Delta T = 1.5$ K around T = 173 K (or equivalently $\Delta T = 12$ K around RT). Similarly, a PbTe cube metasurface reflectarray (a = 1.78 μm, $\Lambda = 2$ μm) on a perfect electric conductor (PEC) substrate exhibits sharp resonances with Qs as high as 4500 (Figure 6c). Utilizing the large associated phase shift around a resonance, drastic phase modulation can be achieved, as depicted in Figure 6c. 2π phase shift is obtained for small temperature modulation $\Delta T \sim 5$ K (around T = 173 K) while maintaining greater than 99% reflectivity. Similar tunability and switching capabilities may be obtained at RT, at the cost of increasing the temperature difference to ∼$\Delta T = 10$ K, which still lay far below other TO modulators. These estimations reveal a great potential for practical TO switching with PbTe components.

2.3 Phase Transition Materials

Among active materials, phase transition and phase change materials can arguably provide the largest variation in optical constants. When applying heat, electric or magnetic fields to these materials, their optical constants can undergo dramatic (and reversible) shifts. Various mechanisms have been investigated and employed to realize tunable nanophotonic and metasurface platforms. These include the transition from nematic to isotropic phases in liquid crystals [31], [32], amorphous to crystalline phase change in GeSbTe (GST) [54], [76], [77] and metal—insulator transitions (MIT)

in prototypical strongly correlated materials such as vanadium dioxide (VO_2) [67], [78]–[82] and V_2O_3 [83], [84].

We have previously demonstrated that VO_2 metasurfaces support switchable dielectric-plasmonic response: in the insulating phase, the metasurfaces exhibit dielectric Mie-type resonances, that are switched to plasmonic resonances in the metallic phase. In the following, we show that hybrid dielectric−VO_2 structures exhibit several novel behaviors of great interest in the development of reconfigurable optics, including independent tuning of the reflection amplitude and phase, large modulation of transmission and absorption, and electronic switching. The device is basically a tunable Fabry–Pérot (TFP) cavity, comprised of a 1 μm thick Ge layer, atop of a 100 nm thick film of VO_2, on an R-cut sapphire substrate (Figure 7a). At the interface between a transparent material and VO_2, the reflectivity undergoes a π phase shift across the MIT. Here, reflection-phase switching of the MIT, modulates the complex reflectivity (i.e., amplitude and phase), transmission, and absorption of the simple Ge−VO_2 TFP. Unlike existing switchable VO_2 photonic devices, here the mesoscopic continuous nature of the MIT in the VO_2 thin film, is used to achieve continuous reflection modulation (Figure 7a), as well as independent control over the phase, a key requirement for reconfigurable high-efficiency metasurfaces. Figure 7b presents characteristic reflection spectra for the fully insulating and metallic phases. When the underlying VO_2 film is in its insulating phase (blue line), the cavity exhibits a broadband low-loss infrared FP spectrum. When the VO_2 is switched to the metallic phase (red line), the spectrum inverts, due to the additional π reflection phase imposed at the Ge−VO_2 interface. Thus, local reflection maxima become minima and vice versa, providing large-magnitude (10%−70%) switching of reflection amplitudes.

To demonstrate the capabilities of continuous modulation, we experimentally measure the reflection amplitude and phase, using a custom-built MIR Michaelson interferometer [50], [85], and compare the results against calculations using the transfer-matrix method (Figure 8). The measured reflectivities of the TFP across the MIT exhibit smooth, continuous variations. At TFP nodes, the points at which the fully insulating and fully metallic states intersect in Figure 7b, the reflection amplitude is unchanged between the extremes, with a suppression at intermediate temperatures due to increased absorption as VO_2 passes through the epsilon-near zero regime [67], [86]–[88] (Figure 8a). At the anti-nodes, on the other hand, there is a large, continuous amplitude shift as the TFP switches between fully insulating and fully metallic regimes (Figure 8b). This behavior largely originates from a continuous modulation of reflection phase at the Ge−VO_2 interface, which is confirmed by calculations using our previously derived VO_2 optical constants [67]. Overall, calculated reflectance shows good agreement with experiment.

The TFP can also operate as a phase modulator, as depicted in Figure 8c. At the TFP nodes, a very small change in amplitude is accompanied by a continuous phase shift of approximately 0.7 radians (40 degrees). The observed phase shift could be further enhanced through a more sophisticated design that involves distributed-Bragg-reflectors or by patterning the Ge layer to form Mie resonators. Nevertheless, the TFP has dual and independent operation mode: amplitude modulation at antinode points and phase modulation at the nodes.

To further demonstrate the applicability of the Ge-VO_2 TFP for local modulation of optical properties, as required for reconfigurable meta-optics, we demonstrate electrically controlled devices. The TFP is modulated through Joule heating by passing current directly through a 200 μm × 200 μm TFP (Figure 7b inset). In the VO2 insulating state, current passes predominantly through the lightly doped Ge layer. This enables Joule heating of the device in both metallic and insulating VO2 states, without introducing additional lossy metals. Figure 9a presents reflection spectra of an electrically controlled TFP for increasing DC currents, captured by an infrared microscope coupled to an FTIR spectrometer. To reduce the amount of power needed to induce the phase transition, the sample is held just below the MIT at 57 °C. The spectra are almost identical to thermally induced TFP of Figure 7b. Here however, we present the continuous tuning of reflection, increasing current values from insulating through intermediate states culminating in a fully metallic phase at I = 105 mA. The temporal characteristics of the device are also investigated by exciting the TFP with a square voltage pulse (26 Vpp, 60 μs), and monitoring the temporal response of the device with a fast MCT detector and the FTIR in a step-scan mode. Figure 9b presents the transient reflectivity in
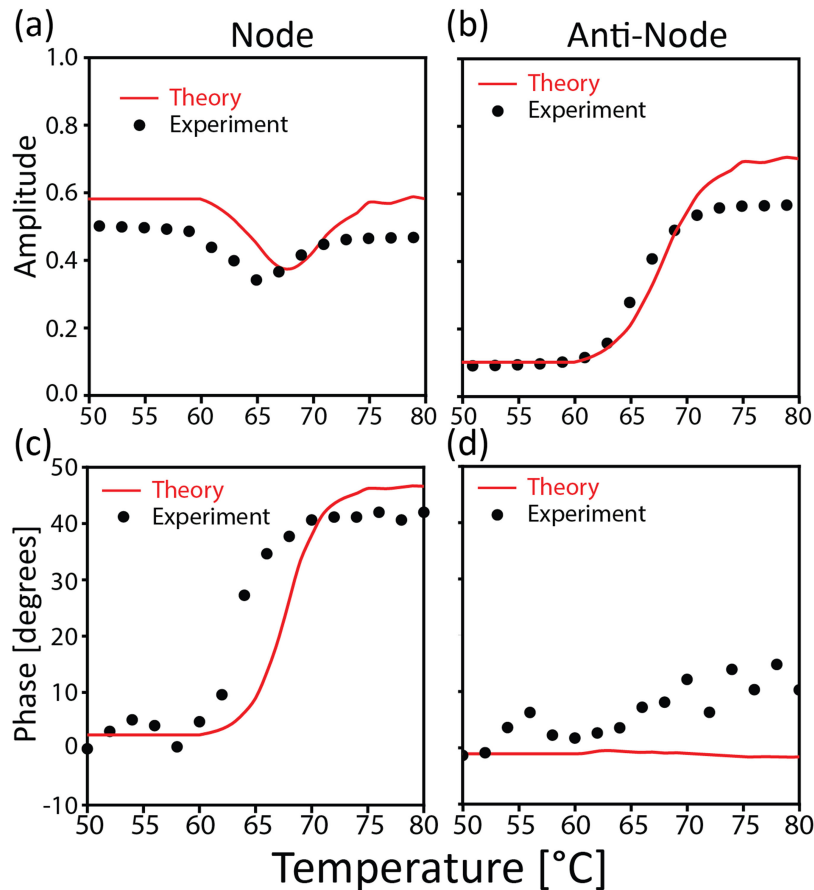
Fig. 8. Amplitude and phase modulation. Reflection amplitude (a, b) and phase (c, d) at a TFP node (a, c) and anti-node (b, d). Here, the anti-node corresponds to 1250 cm^{-1} (8 μm) and the node corresponds to 950 cm^{-1} (10.5 μm). Experimental data are shown as black dots. Calculated predictions, based on fitted VO$_2$ optical constants, are shown as red solid lines.
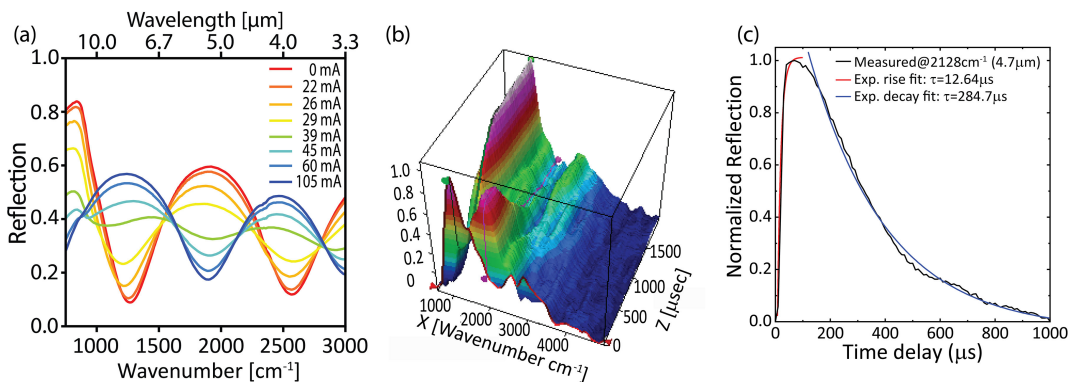

Fig. 9. Electrically tunable Fabry–Pérot. (a) Experimentally measured infrared reflectivity of a TFP, with Ge thickness 850 nm, as the applied DC current is varied, exhibiting continuous electrically tunable reflectivity. (b) Experimentally measured transient reflectivity spectrum of the TFP. (c) Normalized transient reflectivity at the anti-node wavenumber 2128 cm^{-1} ($\lambda = 4.7$ μm) for a 26 V, 60 μs wide square excitation pulse. Solid black line corresponds to the experimental raw data while the red and blue lines correspond to fitted exponential curves (red, heating; blue, cooling).

the 900–4500 cm^{-1} range, exhibiting the continuous temporal evolution of the spectrum, including the nodes and antinodes. Figure 9c traces the rise and decay time characteristics of an antinode at 2128 cm^{-1} ($\lambda = 4.7$ μm). Fast rise time, due to rapid Joule heating is observed, followed by a slower thermal-diffusion-limited decay. Dynamic traces exhibit an approximately 12.65 μs rise time, as determined through an exponential fit with an approximately 285 μs decay time, corresponding to estimated modulation rates on the order of 3.5 kHz. When applying even larger voltages, faster rise times can be achieved [50]. These values are an order of magnitude faster than previous large-area VO$_2$ optical modulators [81], [82] which have rise and relaxation times of the order of few milliseconds. The decay time is likely limited by the relatively large thermal capacitance of the device and may be improved with thermally engineered metasurface structures that reduce the Ge and VO$_2$ volumes. Further improvements in speed can also be attained by reducing the modulation depth or by utilizing vertical contact geometries.

3. Conclusions

In summary, we studied thermal tuning performance in resonators and metasurfaces obtained from several materials systems comprising group IV, group IV-VI semiconductors and phase transition materials. Identifying the linewidth tunability ($\Delta\lambda$/FWHM > 1) as the figure of merit for efficient tuning, we pinpoint the route to achieve such tunability by combings materials with large optical effects along with high-Q resonances. We study TO tuning in Si and Ge and highlight their capabilities with a demonstration of tunable spectral metafilters realized with Si metasurface disk arrays at NIR wavelengths.

To further reduce the temperature gradients required for linewidth tunability, we investigate lead chalcogenides of group IV-VI semiconductors. We show that PbTe is a solution processable material and an excellent candidate for infrared reconfigurable meta-optics, having both high refractive index and largest known TOC of all materials. We find that PbTe exhibits an anomalous TOE with peak performance at cryogenic temperatures, which cannot be explained with standard TOC models. Utilizing peak TOC with high-Q resonances, we demonstrate normalized tunability $\Delta\lambda$/FWHM $= 1.6$ for temperature modulation as small as $\Delta T = 10$ K. We show that when combined into metasurface arrays, this exceptional tunability can be exploited in ultranarrow active notch filers and metasurface phase shifters that require only a few kelvin modulation. These findings demonstrate the enabling potential of PbTe as a versatile, solution-processable, and highly tunable nanophotonic material.

Finally, we investigate tunability in hybrid dielectric$-$VO$_2$ structures and show that these structures exhibit novel properties highly desirable for reconfigurable meta-optics. We utilize the metal$-$insulator phase transition of VO$_2$ to create electrically reconfigurable, continuously tunable nanophotonic devices across a broad spectral range. The continuous modulation is enabled by driving the underlying VO$_2$ film across the phase transition. Additionally, we demonstrate independent modulation of both amplitude and phase at antinodes and nodes of the TFP device. Electronically triggered transient reflection measurements revealed switching rates of 3.5 KHz, which can be further improved with thermal management and more sophisticated designs. These findings expand the potential of active metasurfaces, that take advantage of the reconfigurable properties of hybrid semiconductor$-$VO$_2$ architectures. Altogether, this work highlights the opportunities and potential of thermally tunable semiconductor metasurfaces and can pave the way to efficient high-Q reconfigurable metadevices, which will ultimately be implemented in important applications for the infrared range.

References

[1] N. F. Yu *et al.*, "Light propagation with phase discontinuities: Generalized laws of reflection and refraction," *Science*, vol. 334, pp. 333–337, 2011, doi: 10.1126/science.1210713.

[2] S. Jahani and Z. Jacob, "All-dielectric metamaterials," *Nature Nanotechnol.*, vol. 11, pp. 23–36, 2016, doi: 10.1038/nnano.2015.304.

[3] A. I. Kuznetsov, A. E. Miroshnichenko, M. L. Brongersma, Y. S. Kivshar, and B. Luk'yanchuk, "Optically resonant dielectric nanostructures," *Science*, vol. 354, 2016, Art. no. aag2472, doi: 10.1126/science.aag2472.

[4] A. Arbabi, Y. Horie, M. Bagheri, and A. Faraon, "Dielectric metasurfaces for complete control of phase and polarization with subwavelength spatial resolution and high transmission," *Nature Nanotechnol.*, vol. 10, pp. 937–943, 2015, doi: 10.1038/Nnano.2015.186.

[5] F. Aieta, M. A. Kats, P. Genevet, and F. Capasso, "Multiwavelength achromatic metasurfaces by dispersive phase compensation," *Science*, vol. 347, pp. 1342–1345, 2015, doi: 10.1126/science.aaa2494.

[6] M. Khorasaninejad *et al.*, "Metalenses at visible wavelengths: Diffraction-limited focusing and subwavelength resolution imaging," *Science*, vol. 352, pp. 1190–1194, 2016, doi: 10.1126/science.aaf6644.

[7] E. Arbabi, A. Arbabi, S. M. Kamali, Y. Horie, and A. Faraon, "Controlling the sign of chromatic dispersion in diffractive optics with dielectric metasurfaces," *Optica*, vol. 4, pp. 625–632, 2017, doi: 10.1364/Optica.4.000625.

[8] D. M. Lin, P. Y. Fan, E. Hasman, and M. L. Brongersma, "Dielectric gradient metasurface optical elements," *Science*, vol. 345, pp. 298–302, 2014, doi: 10.1126/science.1253213.

[9] G. H. Yuan, E. T. F. Rogers, and N. I. Zheludev, "Achromatic super-oscillatory lenses with sub-wavelength focusing," *Light, Sci. Appl.*, vol. 6, 2017, Art. no. e17036, doi: ARTN e17036 10.1038/lsa.2017.36.

[10] Y. M. Yang *et al.*, "Nonlinear fano-resonant dielectric metasurfaces," *Nano Lett.*, vol. 15, pp. 7388–7393, 2015, doi: 10.1021/acs.nanolett.5b02802.

[11] D. Smirnova and Y. S. Kivshar, "Multipolar nonlinear nanophotonics," *Optica*, vol. 3, pp. 1241–1255, 2016, doi: 10.1364/optica.3.001241.

[12] S. Liu *et al.*, "Resonantly enhanced second-harmonic generation using III-V semiconductor all-dielectric metasurfaces," *Nano Lett.*, vol. 16, pp. 5426–5432, 2016, doi: 10.1021/acs.nanolett.6b01816.

[13] D. Sell, J. J. Yang, S. Doshay, K. Zhang, and J. A. Fan, "Visible light metasurfaces based on single-crystal silicon," *ACS Photon.*, vol. 3, pp. 1919–1925, 2016, doi: 10.1021/acsphotonics.6b00436.

[14] A. Arbabi, E. Arbabi, Y. Horie, S. M. Kamali, and A. Faraon, "Planar metasurface retroreflector," *Nature Photon.*, vol. 11, pp. 415–420, 2017, doi: 10.1038/Nphoton.2017.96.

[15] K. E. Chong *et al.*, "Polarization-independent silicon metadevices for efficient optical wavefront control," *Nano Lett.*, vol. 15, pp. 5369–5374, 2015, doi: 10.1021/acs.nanolett.5b01752.

[16] M. Decker *et al.*, "High-efficiency dielectric huygens' surfaces," *Adv. Opt. Mater.*, vol. 3, pp. 813–820, 2015, doi: 10.1002/adom.201400584.

[17] Y. M. Yang *et al.*, "Dielectric meta-reflectarray for broadband linear polarization conversion and optical vortex generation," *Nano Lett.*, vol. 14, pp. 1394–1399, 2014, doi: 10.1021/Nl4044482.

[18] M. I. Shalaev *et al.*, "High-efficiency all-dielectric metasurfaces for ultracompact beam manipulation in transmission mode," *Nano Lett.*, vol. 15, pp. 6261–6266, 2015, doi: 10.1021/acs.nanolett.5b02926.

[19] R. C. Devlin, M. Khorasaninejad, W. T. Chen, J. Oh, and F. Capasso, "Broadband high-efficiency dielectric metasurfaces for the visible spectrum," *Proc. Nat. Acad. Sci. United States Amer.*, vol. 113, pp. 10473–10478, 2016, doi: 10.1073/pnas.1611740113.

[20] Z. Li *et al.*, "Dielectric meta-holograms enabled with dual magnetic resonances in visible light," *ACS Nano*, vol. 11, pp. 9382–9389, 2017, doi: 10.1021/acsnano.7b04868.

[21] Z. Xie *et al.*, "Meta-holograms with full parameter control of wavefront over a 1000 nm bandwidth," *ACS Photon.*, vol. 4, pp. 2158–2164, 2017, doi: 10.1021/acsphotonics.7b00710.

[22] P. Spinelli, M. A. Verschuuren, and A. Polman, "Broadband omnidirectional antireflection coating based on subwavelength surface Mie resonators," *Nature Commun.*, vol. 3, 2012, Art. no. 692, doi: Artn 692 Doi 10.1038/Ncomms1691.

[23] S. Liu *et al.*, "Optical magnetic mirrors without metals," *Optica*, vol. 1, pp. 250–256, 2014, doi: 10.1364/Optica.1.000250.

[24] T. Lewi, P. P. Iyer, N. A. Butakov, A. A. Mikhailovsky, and J. A. Schuller, "Widely tunable infrared antennas using free carrier refraction," *Nano Lett.*, vol. 15, pp. 8188–8193, 2015, doi: 10.1021/acs.nanolett.5b03679.

[25] P. P. Iyer, M. Pendharkar, and J. A. Schuller, "Electrically reconfigurable metasurfaces using heterojunction resonators," *Adv. Opt. Mater.*, vol. 4, pp. 1582–1588, 2016, doi: 10.1002/adom.201600297.

[26] S. Makarov *et al.*, "Tuning of magnetic optical response in a dielectric nanoparticle by ultrafast photoexcitation of dense electron-hole plasma," *Nano Lett.*, vol. 15, pp. 6187–6192, 2015, doi: 10.1021/acs.nanolett.5b02534.

[27] M. R. Shcherbakov *et al.*, "Ultrafast all-optical switching with magnetic resonances in nonlinear dielectric nanostructures," *Nano Lett.*, vol. 15, pp. 6985–6990, 2015, doi: 10.1021/acs.nanolett.5b02989.

[28] D. G. Baranov *et al.*, "Nonlinear transient dynamics of photoexcited resonant silicon nanostructures," *ACS Photon.*, vol. 3, pp. 1546–1551, 2016, doi: 10.1021/acsphotonics.6b00358.

[29] M. P. Fischer *et al.*, "Optical activation of germanium plasmonic antennas in the mid-infrared," *Phys. Rev. Lett.*, vol. 117, 2016, Art. no. 047401, doi: 10.1103/PhysRevLett.117.047401.

[30] M. R. Shcherbakov *et al.*, "Ultrafast all-optical tuning of direct-gap semiconductor metasurfaces," *Nature Commun.*, vol. 8, 2017, Art. no. 17, doi: 10.1038/s41467-017-00019-3.

[31] J. Sautter *et al.*, "Active tuning of all-dielectric metasurfaces," *ACS Nano*, vol. 9, pp. 4308–4315, 2015, doi: 10.1021/acsnano.5b00723.

[32] M. Parry *et al.*, "Active tuning of high-Q dielectric metasurfaces," *Appl. Phys. Lett.*, vol. 111, 2017, Art. no. 053102, doi: Artn 053102 10.1063/1.4997301.

[33] J. Bar-David, L. Stern, and U. Levy, "Dynamic control over the optical transmission of nanoscale dielectric metasurface by alkali vapors," *Nano Lett.*, vol. 17, pp. 1127–1131, 2017, doi: 10.1021/acs.nanolett.6b04740.

[34] A. Forouzmand, M. M. Salary, S. Inampudi, and H. Mosallaei, "A tunable multigate indium-tin-oxide-assisted all-dielectric metasurface," *Adv. Opt. Mater.*, vol. 6, 2018, Art. no. 1701275, doi: Artn 1701275 10.1002/Adom.201701275.

[35] A. Howes, W. Y. Wang, I. Kravchenko, and J. Valentine, "Dynamic transmission control based on all-dielectric Huygens metasurfaces," *Optica*, vol. 5, pp. 787–792, 2018, doi: 10.1364/Optica.5.000787.

[36] Q. Wang *et al.*, "Optically reconfigurable metasurfaces and photonic devices based on phase change materials," *Nature Photon.*, vol. 10, pp. 60–65, 2016, doi: 10.1038/nphoton.2015.247.

[37] A. Karvounis, B. Gholipour, K. F. MacDonald, and N. I. Zheludev, "All-dielectric phase-change reconfigurable metasurface," *Appl. Phys. Lett.*, vol. 109, 2016, Art. no. 051103, doi: Artn 051103 10.1063/1.4959272.

[38] C. H. Chu *et al.*, "Active dielectric metasurface based on phase-change medium," *Laser Photon. Rev.*, vol. 10, pp. 986–994, 2016, doi: 10.1002/lpor.201600106.

[39] S. M. Kamali, E. Arbabi, A. Arbabi, Y. Horie, and A. Faraon, "Highly tunable elastic dielectric metasurface lenses," *Laser Photon. Rev.*, vol. 10, pp. 1002–1008, 2016, doi: 10.1002/lpor.201600144.

[40] E. Arbabi *et al.*, "MEMS-tunable dielectric metasurface lens," *Nature Commun.*, vol. 9, 2018, Art. no. 812, doi: 10.1038/s41467-018-03155-6.

[41] A. She, S. Zhang, S. Shian, D. R. Clarke, and F. Capasso, "Adaptive metalenses with simultaneous electrical control of focal length, astigmatism, and shift," *Sci. Adv.*, vol. 4, 2018, Art. no. eaap9957, doi: 10.1126/sciadv.aap9957.

[42] T. Lewi, H. A. Evans, N. A. Butakov, and J. A. Schuller, "Ultrawide thermo-optic tuning of PbTe meta-atoms," *Nano Lett.*, vol. 17, pp. 3940–3945, 2017, doi: 10.1021/acs.nanolett.7b01529.

[43] P. P. Iyer, M. Pendharkar, C. J. Palmstrøm, and J. A. Schuller, "Ultrawide thermal free-carrier tuning of dielectric antennas coupled to epsilon-near-zero substrates," *Nature Commun.*, vol. 8, 2017, Art. no. 472, doi: 10.1038/s41467-017-00615-3.

[44] P. P. Iyer, R. A. DeCrescent, T. Lewi, N. Antonellis, and J. A. Schuller, "Uniform thermo-optic tunability of dielectric metalenses," *Phys. Rev. Appl.*, vol. 10, 2018, Art. no. 044029, doi: 10.1103/PhysRevApplied.10.044029.

[45] M. Rahmani *et al.*, "Reversible thermal tuning of all-dielectric metasurfaces," *Adv. Funct. Mater.*, vol. 27, 2017, Art. no. 1700580, doi: 10.1002/adfm.201700580.

[46] K. Padmaraju, J. Chan, L. Chen, M. Lipson, and K. Bergman, "Thermal stabilization of a microring modulator using feedback control," *Opt. Exp.*, vol. 20, pp. 27999–28008, 2012, doi: 10.1364/oe.20.027999.

[47] J. Sun, E. Timurdogan, A. Yaacobi, E. S. Hosseini, and M. R. Watts, "Large-scale nanophotonic phased array," *Nature*, vol. 493, pp. 195–199, 2013, doi: 10.1038/nature11727.

[48] J. C. Hulme *et al.*, "Fully integrated hybrid silicon two dimensional beam scanner," *Opt. Exp.*, vol. 23, pp. 5861–5874, 2015, doi: 10.1364/OE.23.005861.

[49] B. S. Lee *et al.*, "On-chip thermo-optic tuning of suspended microresonators," *Opt. Exp.*, vol. 25, pp. 12109–12120, 2017, doi: 10.1364/Oe.25.012109.

[50] N. A. Butakov *et al.*, "Broadband electrically tunable dielectric resonators using metal-insulator transitions," *ACS Photon.*, vol. 5, pp. 4056–4060, 2018, doi: 10.1021/acsphotonics.8b00699.

[51] G. Ghosh, *Handbook of Optical Constants of Solids: Handbook of Thermo-Optic Coefficients of Optical Materials with Applications*. New York, NY, USA: Academic, 1998.

[52] T. Lewi, A. Butakov Nikita, and A. Schuller Jon, *Nanophotonics*, vol. 8, pp. 331–338, 2019.

[53] F. S. Ruggeri *et al.*, "Infrared nanospectroscopy characterization of oligomeric and fibrillar aggregates during amyloid formation," *Nature Commun.*, vol. 6, 2015, Art. no. 7831, doi: 10.1038/ncomms8831.

[54] A. Tittl *et al.*, "A switchable mid-infrared plasmonic perfect absorber with multispectral thermal imaging capability," *Adv. Mater.*, vol. 27, pp. 4597–4603, 2015, doi: 10.1002/adma.201502023.

[55] R. Adato and H. Altug, "In-situ ultra-sensitive infrared absorption spectroscopy of biomolecule interactions in real time with plasmonic nanoantennas," *Nature Commun.*, vol. 4, 2013, Art. no. 2154, doi: 10.1038/ncomms3154.

[56] R. Ostendorf *et al.*, "Recent advances and applications of external cavity-QCLs towards hyperspectral imaging for stand-off detection and real-time spectroscopic sensing of chemicals," *Photonics*, vol. 3, 2016, Paper 28, doi: 10.3390/photonics3020028.

[57] T. Lewi and A. Katzir, "Silver halide single-mode strip waveguides for the mid-infrared," *Opt. Lett.*, vol. 37, pp. 2733–2735, 2012, doi: 10.1364/OL.37.002733.

[58] S. Zilberman, A. Ravid, A. Katzir, and T. Lewi, "Fiber-optic evanescent wave spectroscopy of subsurface layers of solid propellant combustion," *J. Propulsion Power*, vol. 32, pp. 1119–1123, 2016, doi: 10.2514/1.B35956.

[59] B. Lobel, O. Eyal, N. Kariv, and A. Katzir, "Temperature controlled CO_2 laser welding of soft tissues: Urinary bladder welding in different animal models (rats, rabbits, and cats)," *Lasers Surgery Medicine*, vol. 26, pp. 4–12, 2000, doi: 10.1002/(SICI)1096-9101(2000)26:1<4::AID-LSM3>3.0.CO;2-J.

[60] Y. Yao, A. J. Hoffman, and C. F. Gmachl, "Mid-infrared quantum cascade lasers," *Nature Photon.*, vol. 6, pp. 432–439, 2012, doi: 10.1038/nphoton.2012.143.

[61] T. Lewi, S. Shalem, A. Tsun, and A. Katzir, "Silver halide single-mode fibers with improved properties in the middle infrared," *Appl. Phys. Lett.*, vol. 91, 2007, Art. no. 251112, doi: 10.1063/1.2827195.

[62] T. Lewi, A. Tsun, A. Katzir, J. Kaster, and F. Fuchs, "Silver halide single mode fibers for broadband middle infrared stellar interferometry," *Appl. Phys. Lett.*, vol. 94, 2009, Art. no. 261105, doi: 10.1063/1.3166864.

[63] T. Lewi, J. Ofek, and A. Katzir, "Antiresonant reflecting microstructured optical fibers for the mid-infrared," *Appl. Phys. Lett.*, vol. 102, 2013, Art. no. 101104, doi: 10.1063/1.4795533.

[64] H.-D. Nguyen *et al.*, "Low-loss 3D-laser-written mid-infrared LiNbO3 depressed-index cladding waveguides for both TE and TM polarizations," *Opt. Exp.*, vol. 25, pp. 3722–3736, 2017, doi: 10.1364/OE.25.003722.

[65] S. Dasgupta, N. G. R. Broderick, D. J. Richardson, T. Lewi, and A. Katzir, "Improved method for estimating the minimum length of modal filters fabricated for stellar interferometry," *Opt. Exp.*, vol. 17, pp. 1935–1946, 2009, doi: 10.1364/OE.17.001935.

[66] R. Grille *et al.*, "Comparative study of mid-infrared fibers for modal filtering," *Appl. Opt.*, vol. 49, pp. 6340–6347, 2010, doi: 10.1364/AO.49.006340.

[67] N. A. Butakov *et al.*, "Switchable plasmonic–Dielectric resonators with metal–insulator transitions," *ACS Photon.*, vol. 5, pp. 371–377, 2017, doi: 10.1021/acsphotonics.7b00334.

[68] J. N. Zemel, J. D. Jensen, and R. B. Schoolar, "Electrical and optical properties of epitaxial films of Pbs Pbse Pbte and Snte," *Phys. Rev.*, vol. 140, pp. 330–335, 1965, doi: 10.1103/PhysRev.140.A330.

[69] Z. M. Gibbs *et al.*, "Temperature dependent band gap in PbX (X = S, Se, Te)," *Appl. Phys. Lett.*, vol. 103, 2013, Art. no. 262109, doi: Artn 262109 10.1063/1.4858195.

[70] E. H. Sargent, "Infrared photovoltaics made by solution processing," *Nature Photon.*, vol. 3, pp. 325–331, 2009, doi: 10.1038/Nphoton.2009.89.

[71] D. Ding *et al.*, "Interface engineering in solution-processed nanocrystal thin films for improved thermoelectric performance," *Adv. Mater.*, vol. 29, 2017, doi: 10.1002/adma.201603444.

[72] E. Xifre-Perez *et al.*, "Mirror-image-induced magnetic modes," *ACS Nano*, vol. 7, pp. 664–668, 2013, doi: 10.1021/nn304855t.

[73] N. Piccioli, J. M. Besson, and M. Balkanski, "Optical-constants and band-gap of Pbte from thin-film studies between 25 and 300 degrees K," *J. Phys. Chem. Solids*, vol. 35, pp. 971–977, 1974, doi: 10.1016/S0022-3697(74)80107-1.

[74] F. Weiting and Y. Yixun, "Temperature effects on the refractive-index of lead-telluride and zinc selenide," *Infrared Phys.*, vol. 30, pp. 371–373, 1990, doi: 10.1016/0020-0891(90)90055-Z.

[75] R. N. Tauber, A. A. Machonis, and I. B. Cadoff, "Thermal and optical energy gaps in PbTe," *J. Appl. Phys.*, vol. 37, pp. 4855–4860, 1966, doi: http://dx.doi.org/10.1063/1.1708150.

[76] M. Wuttig, H. Bhaskaran, and T. Taubner, "Phase-change materials for non-volatile photonic applications," *Nature Photon.*, vol. 11, pp. 465–476, 2017, doi: 10.1038/nphoton.2017.126.

[77] P. Li *et al.*, "Reversible optical switching of highly confined phonon–polaritons with an ultrathin phase-change material," *Nature Mater.*, vol. 15, pp. 870–875, 2016, doi: 10.1038/nmat4649.

[78] M. D. Goldflam *et al.*, "Voltage switching of a VO2 memory metasurface using ionic gel," *Appl. Phys. Lett.*, vol. 105, 2014, Art. no. 041117, doi: 10.1063/1.4891765.

[79] J. Rensberg *et al.*, "Active optical metasurfaces based on defect-engineered phase-transition materials," *Nano Lett.*, vol. 16, pp. 1050–1055, 2016, doi: 10.1021/acs.nanolett.5b04122.

[80] M. Liu *et al.,* "Terahertz-field-induced insulator-to-metal transition in vanadium dioxide metamaterial," *Nature*, vol. 487, pp. 345–348, 2012, doi: 10.1038/nature11231.

[81] Z. Zhu, P. G. Evans, R. F. Haglund, and J. G. Valentine, "Dynamically reconfigurable metadevice employing nanostructured phase-change materials," *Nano Lett.*, vol. 17, pp. 4881–4885, 2017, doi: 10.1021/acs.nanolett.7b01767.

[82] L. Liu, L. Kang, T. S. Mayer, and D. H. Werner, "Hybrid metamaterials for electrically triggered multifunctional control," *Nature Commun.*, vol. 7, 2016, Art. no. 13236, doi: 10.1038/ncomms13236.

[83] Y. Kalcheim *et al.*, "Robust coupling between structural and electronic transitions in a mott material," *Phys. Rev. Lett.*, vol. 122, 2019, Art. no. 057601, doi: 10.1103/PhysRevLett.122.057601.

[84] A. S. McLeod *et al.*, "Nanotextured phase coexistence in the correlated insulator V2O3," *Nature Phys.*, vol. 13, pp. 80–86, 2016, doi: 10.1038/nphys3882.

[85] M. C. Sherrott *et al.*, "Experimental demonstration of >230° phase modulation in gate-tunable graphene–gold reconfigurable mid-infrared metasurfaces," *Nano Lett.*, vol. 17, pp. 3027–3034, 2017, doi: 10.1021/acs.nanolett.7b00359.

[86] N. A. Butakov and J. A. Schuller, "Hybrid optical antennas with photonic resistors," *Opt. Exp.*, vol. 23, pp. 29698–29707, 2015, doi: 10.1364/OE.23.029698.

[87] J. Park, J.-H. Kang, X. Liu, and M. L. Brongersma, "Electrically tunable epsilon-near-zero (ENZ) metafilm absorbers," *Sci. Rep.*, vol. 5, 2015, Art. no. 15754, doi: 10.1038/srep15754.

[88] Y.-W. Huang *et al.*, "Gate-tunable conducting oxide metasurfaces," *Nano Lett.*, vol. 16, pp. 5319–5325, 2016, doi: 10.1021/acs.nanolett.6b00555.